

Porosity-elastic rebound along the Landers 1992 earthquake surface rupture

by

Gilles Peltzer, Paul Rosen, Francois Rogez

Jet Propulsion Laboratory, California Institute of Technology, Pasadena, CA.

and

K. Hudnut, U.S. Geological Survey, Pasadena, CA.

Submitted to JGR on February 12, 1998

Revised: June 16, 1998

Please address correspondence to:

Gilles Peltzer

JPL/MS 183-501

4800 Oak Grove Drive

Pasadena, CA 91109

Tel. (818) 354-75 39, Fax (818)354 94 76

Email: gilles@altyn.jpl.nasa.gov

Abstract Maps of post-seismic surface displacement after the 1992, Landers, California earthquake, generated by interferometric processing of ERS-1 Synthetic Aperture Radar (SAR) images, reveal effects of various deformation processes near the 1992 surface rupture. The large scale pattern of the post-seismic displacement field is a pair of large lobes, mostly visible on the west side of the fault, comparable in shape with the lobes observed in the co-seismic displacement field. This pattern and the steep displacement gradient observed near the Emerson-Camprock fault cannot be simply explained by after-slip on deep sections of the 1992 fault. Models show that horizontal slip occurring on a buried dislocation in a Poisson's material produces a characteristic quadripole pattern in the surface displacement field with several centimeters of vertical motion at distances of 10-20 km from the fault, a pattern that is not observed in the post-seismic interferograms. Considering the large, vertical static displacement produced during the earthquake by compression and stretching of the rocks adjacent to the fault, we propose that post-seismic rebound caused by pore fluid flow may occur over such distances from the fault and compensate vertical ground shift produced by fault after-slip. Such a post-seismic rebound is explained by the change of the shallow crustal rocks Poisson's ratio value from undrained to drained conditions as pore pressure gradients produced by the earthquake dissipate. We show that the combined effects on surface displacement of after-slip on the fault and post-seismic rebound can produce the observed range change in the SAR data. Post-seismic rebound caused by pore fluid flow is also advocated to explain the range decrease (uplift) observed in two pull-apart structures, and range increase (subsidence), observed in a compressional jog of the 1992 rupture. SAR data covering various time intervals indicate that the characteristic time associated with this process is 0.75 ± 0.12 years. A model of the post-seismic rebound in the Homestead Valley pull-apart using Poisson's ratio values of 0.3 and 0.4 for the drained and undrained gouge rocks, respectively accounts for the observed surface uplift in the 3.5 years following the earthquake. The large value inferred for the undrained Poisson's ratio is equivalent to a

seismic velocity ratio V_p/V_s of ~ 2.5 , consistent with the observed low V_s values of fault-zone guided waves at shallow depth (Li et al., 1997). SAR data also reveal post-seismic creep along shallow patches of the Eureka Peak and Burnt Mountain faults with a characteristic decay time of 0.8 years. Co-seismic, dilatant hardening (locking process) followed by post-seismic, pore pressure controlled fault creep provide a plausible mechanism to account for the decay time of the observed slip rate along this section of the fault. The radar data also confirm the absence of fault after-slip along the southern section of the Homestead Valley fault and between the Eureka Peak and Johnson Valley faults, the two sections of the 1992 Landers surface breaks where co-seismic, right-lateral surface slip dropped to zero.

Introduction

The M7.5, Landers earthquake of 28 June 1992 produced a 75 km long surface rupture with ~ 3 m average and up to 6.2 meters of right-lateral displacement (Figure 1) (Hart et al., 1992; Sieh et al., 1992). In the months and years following the earthquake, post-seismic surface displacement has been monitored by repeated surveys of GPS networks, trilateration arrays and creep-meters. Fault slip models based on the GPS data in the first year after the earthquake indicate that less than 10 cm of post-seismic displacement occurred along the northern and central sections of the fault, and up to 18 cm, along the southern Johnson Valley and Eureka Peak faults [Shen et al., 1994]. This amount of after-slip accounts for a post-seismic strain release equivalent to 15% of the co-seismic moment, and is associated with a decay time of 34 days [Shen et al., 1994]. Data recorded by remote (65-100 km) stations of the Southern California Permanent GPS Geodetic array (PGGA) also show post-seismic displacement of up to 15% of the co-seismic signal [Bock et al., 1997; Wdonwinski et al., 1997]. Post-seismic displacements of the nearest sites indicate a decay time of 22 ± 10 days, consistent with the previous estimate made by Shen et al. [1994], superimposed on a longer-term, interseismic trend [Wdonwinski et al., 1997]. Savage and Svarc [1997] interpreted surface displacement data from a linear GPS array across the Emerson fault in the 3.4 years after the earthquake as resulting from up to 1 m of right-lateral slip on the section of the fault below a depth of 10 km. The temporal behavior of their data is described by a short-term (84 ± 23 days) exponential relaxation superimposed on an apparently linear trend. Surveys of small aperture trilateration arrays revealed minor horizontal displacement across the 1992 surface rupture in the 5 months following the earthquake. Virtually no displacement was recorded along the Emerson Camp-Rock fault, ~ 9 mm along the Johnson Valley fault and up to 40 mm along the Eureka Peak fault [Sylvester, 1993]. Creepmeters installed on the Eureka Peak fault after the earthquake have recorded up to 23 cm of surface slip in one year [Behr et al., 1994].

However, except the continuous GPS measurements at remote stations of the PGGA, all instruments listed above provide no or poor estimates of the vertical displacement of the ground. Furthermore, point positioning geodetic techniques are limited by the spatial range they are able to sample given the number and spacing of geodetic monuments they use. In this paper we take a new look at post-seismic processes using surface displacement maps of the Landers 1992 earthquake area generated by SAR interferometry (InSAR). The advantages and complementary character of SAR interferometry are to provide a quasi-continuous view of the displacement field over broad areas, allowing us to detect and analyze surface displacement patterns of various spatial scales, and to have a great sensitivity to vertical ground displacement. The largest post-seismic ground displacements and displacement gradients observed in the radar maps lie within 10 km from the 1992 surface break, a scale both too short for being observed using the existing GPS arrays and too large for being observed in the trilateration and creep-meter data. In a first section we briefly describe the approach and the data analysis strategy for the detection of slow deformation processes. In the following sections we discuss successively (1) after-slip on the Emerson-Camprock fault, (2) post-seismic rebound in fault step-overs, and (3) surface creep along the southern sections of the 1992 break.

Approach

The technique of SAR interferometry consists in combining two SAR complex images of a given area to form an interferogram [Gabriel et al., 1989]. The phase of each pixel in the interferogram is the difference between the phase of the corresponding pixels in each of the two original images. Using appropriate corrections, the phase variations in the interferogram depict variations in the topography across the scene and any displacement of the surface in the direction of the satellite line of sight. If the images are acquired simultaneously, or if the surface did not move between the times of image acquisition, an elevation map can be produced from the interferogram [Zebker et al., 1994a; Rosen et al.,

1995]. If some ground displacement occurred at the surface during the time interval spanned by the SAR images, a line of sight surface change map can be obtained by removing the topographic signal from the interferogram. This can be achieved by either simulating the topographic phase using a digital elevation model (2-pass method, e.g., Massonnet et al. [1993]; Murakami et al. [1996]) or by generating two interferograms out of three or four SAR images of the same area, and computing the phase difference of the two (3- or 4-pass method, e.g., Gabriel et al. [1989]; Zebker et al. [1994b]; Peltzer and Rosen [1995]). The difference of the two phase fields, once scaled to the same sensitivity to topography by the ratio of their baselines, eliminates the topographic phase signal common to both interferograms. In the absence of additional signal such as that produced by variations of the phase propagation delay in the wet troposphere [Goldstein, 1996; Zebker et al., 1997], the remainder is a map of the component of the surface displacement field parallel to the radar line of sight.

To measure surface deformation related to slow deformation processes such as post-seismic displacements, we first select a pair of SAR images spanning a long time interval (change pair) in order to integrate surface deformation over sufficient time to be detectable by the radar, and having a small spatial baseline to minimize the sensitivity to topography. The topographic phase is removed using another image pair (topographic pair) formed with either a third image and one of the two first images (3-pass) or with two independent images (4-pass). We preferably select images close in time for the topographic pair to minimize temporal decorrelation and unrelated surface motion signal, and with a spatial baseline larger than the baseline of the change pair to ensure a good sensitivity to topography. For change pairs with a spatial baseline lower than 20 m, we found the USGS 90 m-digital elevation model accurate enough to remove the topographic phase using the 2-pass approach.

Analysis of Near Field, Post-seismic Deformation

We analyzed SAR data acquired from the ERS tracks 399 and 127, which both cover the Landers earthquake area. The time intervals spanned by the data are shown in Figure 2. The images cover the East California Shear Zone, formed of several NW-SE, strike-slip faults, including the Emerson-Camprock and the Johnson Valley faults that ruptured during the 1992 earthquake. Geologic and geodetic data indicate that the shear zone accommodates ~15% of the Pacific-North America plate motion [Dokka and Travis, 1990; Savage et al., 1990; Sauber et al., 1994]. If approximately 10 mm/yr of right-lateral shear are distributed across the 100 km wide, NW-SE shear zone, such a rate would project into a line of sight displacement rate of 3.2 mm/yr. In three years, this change rate would imply 9.6 mm (1/3 of a phase cycle) of line of sight displacement, distributed across the 100 km wide SAR swath. Although it should be taken into account by proper modeling in the analysis of the far field post-seismic displacements, the small amplitude of the long-term signal and the width over which it is distributed suggest that such a correction is not required for the near and intermediate field displacement analysis presented here.

Figure 3 shows the interferogram covering the time interval between 27 September, 1992 and 23 January, 1996. Surface deformation patterns of various spatial scales are visible in the interferogram. (1) A large lobe, west of the Emerson-Camprock fault indicates that the ground moved away from the satellite in this area. Preliminary interpretations of this pattern suggested that it might be due to after-slip on deep sections of the fault [Massonet et al., 1996; Peltzer et al., 1996a]. (2) Zones of large strain concentrated in the step-overs of the 1992 rupture have been explained by post-seismic rebound caused by the dissipation of the pore fluid pressure gradients produced by the earthquake in the few years following the event [Peltzer et al., 1996b]. (3) Sharp phase cuts observed along the Eureka Peak and Burnt Mountain faults indicate that these faults underwent post-seismic surface creep [Peltzer et al., 1996a]. In the following sub-sections we

discuss in more detail these features of the post-seismic displacement field, and compare them with GPS data and predictions of simple models.

Right-lateral After-slip on the Emerson-Camp Rock Fault

Right-lateral after-slip has been advocated to explain the surface displacement observations after the Landers, 1992 earthquake made with both campaign GPS measurements [Shen et al., 1994; Savage and Svarc, 1997] and continuous GPS measurements at remote PPGA stations [Bock et al., 1997; Wdonwinski et al., 1997]. Savage and Svarc [1997] proposed a model of after-slip based on repeated GPS measurements of a 40 km-long transect across the Emerson fault in the 3.4 years after the earthquake (Figure 3). The GPS array runs through the area where distributed movement is observed in the SAR data, and crosses the 1992 rupture a few kilometers south of the compressive jog of the Emerson-Camprock fault where post-seismic subsidence was observed during the same time period [Peltzer et al., 1996b]. Figure 4 shows range change profiles for 7 different time intervals (Profile 1 in Figure 3) running approximately parallel to the GPS array used by Savage and Svarc [1997]. The discrepancies between these profiles result from the sensitivity of SAR measurements to error sources such as variations in tropospheric conditions, surface conditions and possible orbital errors. For example, the large bump observed in profiles 2 and 3 between 10 and 20 km east of the fault is a topography residual that is probably caused by an anomalous phase propagation delay in the image of September 27, 1992. In fact, water vapor density in the lower atmosphere decreases exponentially with increasing elevation [Gill, 1982] such that changes in atmospheric conditions between the epochs of data acquisitions produce a signal that, in some instances, correlates with topography. The phase appears to be generally noisier in the 15 km-long section west of the fault than along other sections of the profiles. This region corresponds to the area where Zebker et al. [1994b] observed random surface cracks in the co-seismic interferogram. Nevertheless, several features appear to be stable between

these profiles and can be related with confidence to actual ground displacements in the 4 years following the Landers earthquake. All profiles clearly show that the ground moved away from the satellite west of the fault and toward the satellite east of it, a pattern that is apparently consistent with right-lateral shear parallel to the fault [Massonet et al., 1996, Peltzer et al., 1996a]. Overall, the displacement profiles are relatively symmetric with respect to a point slightly east of the 1992 surface break, with a maximum amplitude of approximately 5% of the co-seismic signal amplitude in the four years following the earthquake. The profiles also show a steep displacement gradient in the 1-5 km section east of the 1992 surface break, with an amplitude depending on both the starting date and the duration of the corresponding time interval. A decay time of 1.6 ± 0.4 years can be derived by fitting the amplitude data to an exponentially decaying function. If these characteristics of the observed range change were due to pure, right-lateral shear parallel to the direction of the fault, the amplitude and steep gradient near the fault would require a source as shallow as 1.5 km and approximately 0.3 m of right-lateral after-slip [Peltzer et al., 1996a].

However, we argue below that the steep gradient and part of the observed range change near the fault are more likely due to vertical motion induced by post-seismic, poro-elastic rebound rather than due to right-lateral shear as previously inferred. The argument is based on the general result of elastic modeling that any distribution of horizontal slip on a vertical dislocation buried in an elastic medium will produce four lobes of vertical displacement at the surface in the four quadrants determined by the fault and its perpendicular direction. Because the SAR is more sensitive to vertical ground shifts than it is to horizontal displacements, if after-slip were the only post-seismic process to account for the observed displacement field, such lobes should be prominent in the interferograms. They are not observed in the SAR data.

Comparison between SAR data, GPS data, and after-slip model

To compare the displacements measured by GPS along the transect across the Emerson-Camprock fault (diamonds in Figure 3) with the SAR data (profile 1, Figure 3), we projected onto the radar line of sight both the horizontal and vertical components of the GPS-estimated vectors (Table 1 and Figure 6b in Savage and Svarc [1997]) after appropriate scaling for matching the observation time period of the SAR data (Figure 5a). Unfortunately this comparison appeared to be meaningless because of the quite large error bars of the vertical displacement rate estimates in the GPS data. Because the ERS SAR line of sight incidence angle at mid-swath is 23° off the vertical, the ± 12 mm/yr error bars on the vertical rates obtained with the GPS lead to ± 5 cm of error in range change over the 4 years of observation with the SAR, an error that is larger than the largest signal observed along the profile in the SAR data (Figure 5a). The line of sight projection of the horizontal components of GPS vectors however, seems to be in agreement with the SAR range change in the far field but a large discrepancy between the two data sets occurs within 10 km from the fault, where vertical motion is likely to have taken place.

Savage and Svarc [1997] interpreted the signal seen with seven surveys of the GPS array in the first 3.4 years after the earthquake as being caused by right-lateral after-slip on the downward projection of the 1992 rupture plane between depths of 10 and 30 km. The preferred after-slip solution (Model A) of Savage and Svarc's [1997] inversion implies up to 1 m of slip on the Emerson section of the fault. A comparison between the line of sight surface displacement profile observed in the SAR data and that predicted by this model shows evident inconsistency (Figure 5b). The polarities of the two profiles are opposed: the SAR data indicate a range increase (movement away from the satellite) west of the fault and range decrease (movement toward the satellite) east of it; the model predicts the opposite. Figure 5b also shows the independent contributions of the vertical and horizontal components of the displacement predicted by the model to the range change profile. It is clear that the line of sight displacement is dominated by the vertical surface motion, a

contribution that is ignored in Savage and Svarc's [1997] inversion because of the poor accuracy of the GPS data in the vertical.

Poro-elastic rebound

If after-slip has to be advocated to explain the right-lateral shear parallel to the fault observed in the GPS horizontal displacement vectors [Savage and Svarc, 1997], one has to explain why the contribution of the vertical motion predicted by the model is not depicted in the SAR data. A possible way of reconciling after-slip models and SAR observations is to advocate a post-seismic rebound due to pore fluid flow in the shallow crust. As in the fault step overs [Peltzer et al., 1996b], the volume of rocks adjacent to the fault undergoes compression or stretching during the earthquake that result in vertical movement of the ground. Because the Poisson's ratio of a porous rock is larger under undrained conditions (co-seismic) than it is under drained conditions (post-seismic) [e.g., MacKenzie, 1950; Sato, 1952; Rice and Cleary, 1976], the post-seismic relaxation of the pore fluid pressure gradients induced by the co-seismic volume change of the country rock produces a vertical rebound that is proportional to the co-seismic vertical motion and opposite in sign. As in the case of a pull-apart structure [Peltzer et al., 1996b], if a volume of rock experiences horizontal stretching ϵ , the resulting vertical ground motion is

$$S_u = -v_u \epsilon h \quad (1)$$

where v_u is the undrained Poisson's ratio and h is the thickness of the intervening layer. As time passes after the earthquake, fluid flow allows pore pressure gradients to dissipate, and the volume of rock eventually reaches a drained condition. After hydrostatic equilibrium is achieved, the residual subsidence is

$$S_d = -v_d \epsilon h \quad (2)$$

where v_d is the drained Poisson's ratio of the rock. The post-seismic vertical displacement of the ground is then

$$U = S_u - S_d = - (1 - v_d/v_u) S_u . \quad (3)$$

For a strike-slip dislocation most of the vertical motion occurring near the fault results from the compression and stretching of the adjacent rocks. Therefore, the observation of the co-seismic vertical movement of the ground can be used to predict the amplitude of the post-seismic rebound. In the case of the 1992 Landers earthquake, there is no geodetic data providing information on the vertical component of the static displacement of the ground near the fault. However, the comparison of co-seismic interferometric maps with predictions of simple, elastic half-space models indicates that such a formulation predicts accurately the observed co-seismic displacement in the intermediate and far field of the dislocation [e.g., Massonet et al., 1993]. Figure 5c shows the projection on the range change profile of the vertical displacement predicted by the joint inversion model of Wald and Heaton [1994]. Such a curve indicates that, near the Emerson-Camprock fault, the country rocks experienced compression west of the fault and extension east of it. Using equation (3) and the reasonable values of $v_d=0.27$ and $v_u=0.33$ for the drained and undrained Poisson's ratio, respectively [Rice and Cleary, 1976], one can predict the post-seismic rebound along the transect (Figure 5c). The combination of this rebound and the range change predicted by Savage and Svarc's [1997] Model A (Figure 5b) results in a range change profile bearing the same polarity and comparable amplitude as the range change profile observed in the SAR data (Figure 5c). However, this combined model produces a steep gradient in the profile exactly at the fault (Figure 5c), unlike the observed profile where the steep gradient appears to occur between 1 and 5 km east of the 1992 surface break (Figure 5b). Two reasons may be advocated to explain this difference. First, the dashed curve in Figure 5c represents only the vertical component of the poro-elastic rebound. The vertical shift of the surface must be associated with horizontal shifts near the

zone of steep gradient, just as a zone of subsidence would produce radial, convergent horizontal motion of the surface around it. According to this observation, the ground surface within the 5 km east of the fault might have moved toward the west, i.e., away from the radar, as a consequence of the steep rebound gradient at the fault. The effect of this horizontal motion on the range change curve would be to place the zone of steep gradient a couple of kilometers east of the fault trace, as it is observed in the SAR data. It is interesting to note that the GPS data indicate that the two stations located near and east of the fault moved toward the fault in the 3.5 years following the earthquake [Savage and Svarc, 1997], a feature that is not explained by the after-slip model alone. The westward motion of these two sites also explains the fact that the associated range change gradient occurs east, and not at the fault in the projection shown in Figure 5a. Another reason to explain the observed offset gradient is the fact that the surface break has two branches, just north of the studied profile, suggesting that the actual shear may have occurred at depth slightly east of the surface break where the profile intersects with the fault.

Visco-elastic relaxation

An alternative explanation to reconcile the right-lateral shear observed in the GPS horizontal vectors and SAR observations could be that the shear is due to visco-elastic relaxation in the lower crust/upper mantle layers as opposed to resulting from after-slip on the fault. Recent developments of 2-layer gravity models have shown that vertical movements of the surface during the post-seismic relaxation were reduced to a negligible level compared to horizontal movements when gravity was taken into account [Yu et al., 1996; Pollitz, 1997]. Although the effect of gravity may contribute to limiting the vertical displacement at the surface, visco-elastic relaxation is generally associated with time constants much larger than the duration of observation of our data and therefore may not have such a great influence in the first 4 years of the post seismic period. Furthermore, the steep range change gradient observed near the 1992 rupture cannot be accounted for by

such a model that would lead to much broader and smoother surface displacement patterns [Yu et al., 1996; Pollitz, 1997].

Post-seismic Rebound in Fault Step-overs

Intense surface strains were observed in the interferograms along sections of the 1992 surface rupture where the faulting changes direction or comprised two or more overlapping branches that formed pull-apart structures. In the pull-apart basins between the Homestead Valley and Johnson Valley faults and between the Emerson and Homestead valley faults, the observed ground displacement produced range decreases, consistent with surface uplift (Figure 3, 5). In the compressive jog between the Camprock and Emerson faults, the observed displacement produced range increase, consistent with ground subsidence (Figure 3, 6). Analysis of several interferograms covering various time intervals within the 4 years after the earthquake indicates that the decay time associated with this process is 0.75 ± 0.12 years (Figure 7), similar to the characteristic time describing earthquake-associated phenomena that are often explained by pore fluid flow in the upper crust [Nur and Booker, 1972; Booker, 1974; Anderson and Whitcomb, 1975; Li et al., 1987; Muir-Wood and King, 1993]. These observations led us to propose that the post-seismic rebound signal observed in fault step-overs were due to changes in mechanical properties of the shallow crustal rocks in the fault zone, as pore pressure gradients caused by the earthquake dissipated [Peltzer et al., 1996b]. Theoretical models of elastic media containing holes [e.g., MacKenzie, 1950; Sato, 1952] and laboratory experiments on a wide variety of crustal rocks [e.g., Rice and Cleary, 1976] indicate that the Poisson's ratio of a porous media under undrained conditions (ν_u) is larger than its value under drained conditions (ν_d). The post-seismic surface motion in a pull-apart is therefore uplift. Conversely, if a volume of rock is subject to compression during an earthquake, such a

process predicts post-seismic subsidence, as it is observed near the Emerson-Camprock fault compressive jog (Figure 6) [Peltzer et al., 1996b].

Using the formulation expressed in Equation (3), we can relate the post-seismic uplift to the co-seismic subsidence produced by rock stretching in a pull-apart structure. The critical scaling parameter is the ratio of the drained and undrained Poisson's ratios. Using the fault slip distribution measured in the field after the Landers earthquake along the Homestead Valley, the Kickapoo and the Johnson Valley faults, we have modeled the co-seismic subsidence and have derived the post-seismic rebound in the Homestead Valley pull apart after Equation (3). The fault model includes 1-2 km-long, 4 km-deep, vertical fault patches aligned with the fault trace mapped in the field [Sieh et al., 1993]. The horizontal, co-seismic slip for each patch is determined by interpolation between data points mapped by Sowers et al. [1994] between latitude 34.28°N and 34.37°N , and by Sieh et al. [1993] and Hart et al. [1993] for the southern section of the Johnson Valley and the northern section of the Homestead Valley fault (Figure 8a). The "slip gap" section in the southern Homestead Valley fault where no surface offset was observed in the field [Sieh et al., 1993; Spotilla and Sieh, 1996] has been assigned a slip of 1 m based on Hudnut et al. [1994] co-seismic slip model.

The areal distribution of the predicted surface uplift agrees relatively well with the observation made in the SAR data (Figure 3, 8a). As expected, the model predicts surface uplift in the valley between the overlapping sections of the 1992 rupture (Figure 8a). The model also predicts surface uplift near the bend in the Johnson Valley fault (Lat. 34.26°N , Figure 8a). The post-seismic motion there may result from the co-seismic strain of the adjacent volume of rock due to the curvature of the fault and the large along-strike variation of the co-seismic slip in this section of the fault (Figure 8a). However, the model also predicts uplift east of the Homestead Valley fault near the northern tip of the Kickapoo fault (Figure 8a), an area where no vertical displacement is observed in the SAR data (Figure 3). Improper modeling of the slip at depth along this complicated section of the 1992 rupture

[e.g. Spotilla and Sieh, 1996] is the most likely explanation for the model failure in this area.

Figure 8b shows the observed and predicted slant range components of displacement along the profile across the Homestead Valley pull apart (Figure 3) using two sets of Poisson's ratios values. First, we have assumed values 0.27 and 0.3 for the drained and undrained Poisson's ratios of the shallow rocks, respectively [Rice and Cleary, 1976; Li et al., 1992; Peltzer et al., 1996b]. These values lead to a ratio $v_d/v_u = 0.9$ implying that the amplitude of the post-seismic uplift is equal to 1/10th of the amplitude of the co-seismic subsidence, accounting for less than 2 cm of vertical uplift in the pull-apart. A greater contrast between undrained and drained Poisson's ratio values would be needed to account for the observed uplift.

Recent seismological studies have revealed anomalously low S-wave velocities and corresponding high V_p/V_s ratios within fault zones at shallow depth [e.g., Michelini and Mc Evilly, 1991; Li et al., 1997]. Reports on fault-zone guided waves from near-surface explosions in the San Andreas fault at Parkfield indicate values of up to 2.5 for the V_p/V_s ratio in the upper 3 km of the fault zone [Li et al., 1997; Y.G. Li, personal communication]. Such low values contrast with crustal velocity values estimated for the overall Mojave block [e.g., Li et al., 1992] and are commonly attributed to intense fracturing, brecciation, and liquid saturation of the gouge rocks within the fault zones. Because the undrained Poisson's ratio is directly related to the ratio of seismic waves velocities V_p/V_s according to

$$\frac{V_p}{V_s} = \sqrt{2 \frac{1 - \nu_u}{1 - 2\nu_u}}, \quad (4)$$

a large V_p/V_s ratio indicates a large value of the undrained Poisson's ratio. In particular, $V_p/V_s = 2.5$ implies $\nu_u = 0.4$. Using the value of 0.4 for the undrained Poisson's ratio, and the values discussed above for other parameters in Equation (3) leads to a post-seismic

uplift of ~ 5 cm in the Homestead Valley pull-apart, in good agreement with the uplift inferred from the SAR data (Figure 8b). This result supports our earlier interpretation that pore fluid transfer provides a plausible mechanism to account for the observed surface movements in the fault step-overs after the Landers, 1992 earthquake [Peltzer et al., 1996b].

Surface Creep Along the Burnt Mountain and Eureka Peak Faults

Sharp phase cuts are readily visible in the interferograms along the Burnt Mountain and the Eureka Peak faults 1992 surface breaks (Figure 3, 9a). These features result from fault creep occurring in the years following the earthquake. Creepmeters installed along the Eureka Peak fault indicated that up to 23 cm of after-slip occurred on the Eureka Peak fault in the first year after the earthquake [Behr et al., 1994]. No instrument was installed on the Burnt Mountain fault and post-seismic creep had not previously been recognized along this fault. The phase profile across the creeping sections of the two faults indicates that after-slip is limited to shallow patches on the faults (Figure 9a). In fact, the distance from the faults over which the displacement vanishes does not exceed 5 km for the Eureka Peak fault and 2 km for the Burnt Mountain faults, corresponding to down-dip widths of the creeping patches of approximately 3 km and 1 km, respectively. The box-profile parallel to the Burnt Mountain fault shows that creep is relatively uniformly distributed along the 9-km long creeping section of the fault and produced ~ 1 -1.5 cm of line of sight displacement. If the observed offset is due to purely horizontal slip on the north-south striking fault, the observed change corresponds to 12-17 cm of right-lateral slip for the observation period spanned by the data of Figure 9. The box-profile parallel to the Eureka Peak fault indicates that slip gradually increases from north to south and abruptly stops near the southern end of the 1992 rupture (Figures 9a). Figure 9b shows the slip distribution along the creeping section of the Eureka Peak fault for the 27 September 1992 - 23 January 1996 and 10 January 1993 - 23 May 1995 time periods, assuming the observed range change

corresponds to purely horizontal strike-slip on the N160°E striking fault [Behr et al., 1994; A. Sylvester, personal communication]. If the observed slip is distributed uniformly over a depth of ~ 3 km, the along-strike slip-distributions shown in Figure 9b correspond to geodetic moments of 9.3×10^{16} Nm and 5.4×10^{16} Nm for the two time periods, respectively. It is interesting to note that the cumulative seismic moments released by aftershocks within 5 km from the Eureka Peak fault during the same time periods are only 9.0×10^{14} and 1.6×10^{14} , respectively, more than two orders of magnitude lower than the corresponding geodetic moments.

The proportionality of the slip distributions for the two intervals shown in Figure 9b indicates a consistent temporal behavior of the slip rate distribution along strike. Using data covering four time intervals between September 1992 and March, 1997, we have adjusted an exponential function of the type

$$w = w_0(1 - e^{-t/\tau}) \quad (5)$$

to the observed after-slip and derived a characteristic time of 0.8 years ($0.55 \text{ years} < \tau < 1.3 \text{ years}$) (Figure 10). As the decay time associated with the post-seismic rebound in the fault step-overs, a decay time of 0.8 years also suggests a possible dependence to fluid flow in the shallow crust. Recent studies have emphasized the role of fluids to explain the behavior of seismic and creeping faults [e.g., Rudnicki and Chen, 1988; Blanpied et al., 1992; Sleep and Blanpied, 1992; Lockner and Byerlee, 1994; Sleep and Blanpied, 1994]. Following these studies, we propose a scenario involving dilatant hardening followed by pore pressure controlled creep to explain the shallow after-slip observed along the Eureka Peak fault. Frictional slip is often accompanied by dilatancy, which cause a local pore pressure decrease and an increase of the effective normal stress on the fault plane, thus inhibiting further slip [Rudnicki and Chen, 1988]. If such a mechanism (dilatant hardening) is responsible for the locking of the shallow part of the Eureka Peak fault during the 1992 earthquake, the following conditions exist immediately after the earthquake: (1) a residual

shear stress equivalent to a quantity of slip D is stored as elastic strain in the country rock over a distance L on each side of the fault (Figure 11), (2) the local pore pressure is below hydrostatic equilibrium. As pore fluid flow gradually restores hydrostatic pressure in the fault zone, the normal stress is released on the fault and creeping begins. As creep goes on, the Coulomb criterion

$$\tau = \tau_0 + C(\sigma_n - p_f) \quad (6)$$

expresses the relation between the shear stress τ and normal stress σ_n on the fault plane, and the local pore pressure p_f . Slip on the fault causes the shear traction to decrease as the post-seismic displacement d increases according to

$$\tau = \mu \frac{D - d}{L} \quad (7)$$

where μ is the elastic shear modulus of the adjacent rocks (Figure 11). If we assume that the normal stress remains constant during the time period of observation, equations (6) and (7) show that d and p_f are linearly related and should therefore have the same time dependence. If the temporal behavior of the pore pressure after the earthquake is described by an exponential increasing function, the post-seismic displacement d must increase similarly with time. By gradually reducing the effective normal stress on the fault, the pore pressure increase controls the creep rate on the fault.

Conclusion

We have analyzed intermediate and near field, post-seismic surface displacements following the Landers, 1992 earthquake using ERS-1 SAR data covering various time intervals between September, 1992 and March, 1997. The interferometric maps revealed transient displacement patterns of various spatial scales that were not or only partially captured by other geodetic techniques. In particular, the SAR maps depict clearly vertical displacement of the surface, a component of the displacement field that has been ignored in

previous studies using conventional geodetic measurements. Analysis of the range change maps covering 4 years after the 1992 earthquake suggests that post-seismic rebound, resulting from the change of the Poisson's ratio value of the strained rocks from undrained to drained conditions as pore fluid flow allows pore pressure gradients caused by the earthquake to dissipate, not only occurred in the fault step-overs of the 1992 rupture [Peltzer et al., 1996b] but also within distance of up to 15 km from the fault, an area where the country rock experienced large pore volume change during the earthquake.

In fact, the combined analysis of GPS and SAR data along the Emerson-Camprock fault array indicates that after-slip models alone cannot account for the observations because they produce vertical displacement patterns that are not observed in the SAR data. We show that the added effects on the displacement field of (1) post-seismic rebound caused by pore fluid flow and (2) after-slip on deep sections of the fault account for the observed displacement near the Emerson-Camprock fault.

Post seismic, vertical rebound was observed in the two pull-apart structures and the compressive jog of the 1992 surface break. Forward modeling of the co-seismic subsidence and the subsequent post-seismic rebound in the Homestead Valley - Johnson Valley faults step-over requires a large undrained Poisson's ratio value ($\nu_u = 0.4$) to successfully account for the observed post-seismic uplift in the pull-apart. Such a high value of ν_u is independently suggested by the observed, anomalously low S-wave velocities in the upper 3-5 km of fault zones, where values as high as 2.5 have been estimated for the V_p/V_s ratio of fault-zone guided waves [Li et al., 1997].

Finally, SAR interferometric maps revealed that two sections of the 1992 rupture, the Eureka Peak fault and the Burnt Mountain fault, have undergone surface creep in the years following the earthquake. Clear cuts in the phase field aligned with the fault traces allowed us to map the along-strike surface-slip distribution along these two faults. A simple model involving dilatant hardening (fault locking process) followed by pore pressure

controlled normal stress release is proposed to explain the similarity between the observed decay time of the creeping process and the relaxation times describing the percolation of fluids in the shallow crust. Along the Eureka Peak fault, the geodetic moment released by after-slip exceeds the cumulative seismic moment released by aftershocks in the vicinity of the fault during the same time periods by more than two orders of magnitude.

The spatial scale of the most intense post-seismic deformation features observed in the radar interferograms ranged from a hundred meters to a few kilometers. Such a scale range appears to be both too small for being observed in the GPS data [e.g., Shen et al., 1994] and too large for affecting small aperture trilateration arrays across the fault [Sylvester, 1993]. Except along the Eureka Peak fault where creep has been monitored in 3 places during the year after the earthquake [Behr et al., 1994], most of the near field, post-seismic deformation observed in the SAR data has been missed by the ground based geodetic techniques. Furthermore, it has been possible to detect the effect of post-seismic fluid flow because of the great sensitivity of SAR measurements to vertical displacements of the ground, a component that was not or poorly estimated with the geodetic techniques used after the Landers earthquake. These remarks emphasize the importance of measuring the three components of the surface displacement field continuously in space along active faults susceptible of generating earthquakes. If measurable precursory transient processes ever occur before some earthquakes, as it has been proposed in several instances [e.g., Allen et al., 1991; Kanamori and Anderson, 1975; Linde et al., 1988; Shifflett et al., 1995; Thurber, 1996], the associated ground movements may have remained undetected because of the inherent limitations of available geodetic techniques [e.g., Johnston et al., 1994]. In that sense, SAR interferometry has a great potential to efficiently complement point positioning geodetic techniques in the study of earthquakes and related processes.

Acknowledgment: We would like to thank E. Ivins for discussions on post-seismic processes. The ERS radar data were provided by the European Space Agency. The work

presented in this paper has been performed at the Jet Propulsion Laboratory, California Institute of Technology under contract with NASA.

Figure captions:

Figure 1. Map of the 28 June 1992, Landers earthquake area. Solid lines is the 28 June, 1992 surface rupture [Sieh et al., 1993]. Shade depicts topography from USGS digital elevation model. White dots are aftershocks between 8/7/92 and 1/23/96 [Hauksson 1993]. Box shows areas covered by SAR data shown in Figure 3.

Figure 2. Time intervals covered by SAR data used in this study. Numbers indicate perpendicular component of baselines (distance between orbits, perpendicular to radar line of sight) in meters at latitude $34^{\circ}20'$.

Figure 3. Interferometric map of the Landers area generated with SAR image covering the 27 September 1992 - 23 January 1996 time period. Colors overlaying backscatter radar image represent ground displacement in the direction of the satellite. Coordinates of vector pointing to ERS satellite at mid-swath in local east-north-up reference frame are 0.381, -0.088, 0.920 [European Space Agency, 1992]. Gray areas are zones where phase could not be unwrapped due to signal decorrelation between two SAR images. Black lines depict 1992 surface rupture. White lines indicate profiles shown in Figures 4, 5, 6 and 9. Yellow diamonds show locations of GPS stations used by Savage and Svarc [1997]. Concentric fringes on left side of image result from M5.4, shallow aftershock of 4 December, 1992 [Feigl et al., 1995].

Figure 4. Line of sight surface displacement along 40 km-long, 800 m-wide profile across Emerson-Camprock fault (profile 1 in Figure 3) observed in 7 interferometric change maps covering time intervals. Numbers refer to corresponding time intervals in Figure 2.

Figure 5a. Comparison of range change along profile 1 between August 7, 1992 and September 24, 1995 observed in SAR data (solid line) with surface displacement estimated

with GPS measurements along Emerson fault transect [Savage and Svarc, 1997]. Light gray dots and bars are projections of 3 components of GPS vectors and error bars along radar line of sight. Dark gray dots and bars are projection of GPS vectors horizontal components only. GPS data are scaled to match time interval covered by radar data the following way: horizontal components (Table 1, Savage and Svarc [1997]) are scaled by $[f(s_2)-f(s_1)]/[f(t_2)-f(t_1)]$, where f is temporal function describing post-seismic GPS displacement [Savage and Svarc, 1997], t_1 and t_2 are epochs of first and last GPS survey of transect and s_1 and s_2 are epochs of SAR passes for data shown; GPS uplift rates (Figure 6 in Savage and Svarc [1997]) are scaled by (s_2-s_1) .

Figure 5b. Line of sight displacement observed in SAR data (solid line) compared with range change predicted by Savage and Svarc's [1997] model A (long dashes) along profile 1 (Figure 3). Dotted (resp. short dashed) line shows line of sight projection of vertical (resp. horizontal) component of surface displacement predicted by model. Modeled curves are scaled as GPS data in Figure 5a.

Figure 5c. Line of sight displacement along profile 1 (Figure 3) produced by (1) vertical component of co-seismic model (dotted line, joint inversion model of Wald and Heaton [1994]), (2) post-seismic rebound produced by pore fluid flow (dashed line), and (3) combination of Savage and Svarc [1997] model A and post-seismic rebound (solid line). Post-seismic rebound is derived from co-seismic vertical displacement using Poisson's ratio values $\nu_d=0.27$ (drained) and $\nu_u=0.33$ (undrained), and scaled using characteristic decaying time $\tau_0=1.6$ years (see text).

Figure 6. Line of sight surface displacement along profiles 2, 3 and 4 shown in Figure 3 for interferograms spanning August 7, 1992 - September 24, 1995 (black), September 27,

1992 - January 23, 1996 (dark gray), and January 10, 1993 - May 25, 1995 (light gray) time intervals. Dots are displacement of individual image pixels within 400 m from profile line and solid curves indicate averaged values in 160 m-long bins along profiles strike. After Peltzer et al. [1996].

Figure 7. Post-seismic surface uplift in Homestead Valley pull-apart plotted as a function of time. Curve is function $w(t) = w_0(1 - e^{-t/\tau})$, adjusted to data ($w_0=6.2$ cm, $\tau=0.75$ years). Solid lines are uplift estimates using SAR data of Figure 5. Vertical bars indicate ± 0.5 cm error on uplift estimates. Dashed lines are same as solid lines, shifted to match adjusted curve $w(t)$.

Figure 8a. Modeled line of sight surface movements resulting from post-seismic pore fluid flow in the shallow crust in the Homestead Valley pull-apart structure (see text). Elastic model is based on co-seismic fault slip distribution shown on the left. Slip data are after Sowers et al. [1994], Sieh et al. [1993], Hart et al. [1993], and Hudnut et al. [1994].

Figure 8b. Observed and predicted line of sight displacement along profile 4 across Homestead Valley pull-apart structure for the 7 August 1992 - 24 September 1995 time period. Light shade and dark shade modeled profiles correspond to ratios of drained to undrained Poisson's ratios ν_d/ν_u of 0.9 and 0.75, respectively.

Figure 9 a. Line of sight surface displacement along profiles across (5) and parallel (6 and 7) to Eureka Peak and Burnt Mountain faults (see location in Figure 3). Phase shift values of individual image pixels in boxes along profiles parallel to faults fall into two groups depending on pixel location with respect to faults. Offset between two population of dots indicates slip distribution along faults.

Figure 9 b. Post-seismic slip distribution observed along Eureka Peak fault for time intervals 27 September 92 - 23 January 1996 (upper curve) and 10 January 1993 - 23 May 1995 (lower curve). Right-lateral component of slip is derived from line of sight displacement assuming purely horizontal strike-slip movement on fault.

Figure 10. Same as Figure 7 for after-slip data along Eureka Peak fault. Exponential curve fit to data indicates a relaxation time of 0.8 years.

Figure 11. 3-D sketch of creeping fault defining parameters D , d , τ , σ_n , and L discussed in text.

References:

- Allen, C.R., Luo Z., Qian H., Wen X., Zhou H., and Huang W., Field study of a highly active fault zone: The Xianshuihe fault of southwestern China, *Geol. Soc. Am. Bull.*, 103, 1178-1199, 1991.
- Anderson, D.L. and J.H. Whitecomb, Time-dependant seismology, *J. Geophys. Res.*, 80, 1497-1503, 1975.
- Behr, J., R. Bilham, P. Bodin, and S. Gross, Eureka Peak fault afterslip following the 28 June 1992 Landers earthquake, *Bull. Seism. Soc. Am.*, 84, 826-834, 1994.
- Blanpied, M.L., D.A. Lockner, and J.D. Byerlee, An earthquake mechanism based on rapid sealing of faults, *Nature*, 574-576, 1992.
- Bock, Y., S. Wdowinski, P. Fang, et al., Southern California Permanent GPS Geodetic Array: Continuous measurements of regional crustal deformation between the 1992 Landers and 1994 Northridge earthquakes, *J. Geophys. Res.*, 102, 18,013-18,034, 1997.
- Booker, R.J., Time dependant strain following faulting of porous medium, *J. Geophys. Res.*, 79, 2037-2044, 1974.
- Dokka, R.K., and C.J. Travis, Late Cenozoic strike-slip faulting in the Mojave Desert, California, *Tectonics*, 2, 311-340, 1990.
- European Space Agency, ERS-1 System, 87 pp., ESA Publi. Div., ESTEC, Noordwijk, The Netherlands, 1992.
- Feigl, K., A. Sergent, and D. Jacq, Estimation of an earthquake focal mechanism from a satellite radar interferogram: Application to the December 4, 1992 Landers aftershock, *Geophys. Res. Lett.*, 22, 1037-1040, 1995.
- Gabriel, A.G., R.M. Goldstein, and H.A. Zebker, Mapping small elevation changes over large areas: Differential radar interferometry, *J. Geophys. Res.*, 94, 9183-9191, 1989.
- Gill, A.E., *Atmosphere-Ocean Dynamics*, Academic Press, New York, 662p., 1982.

- Goldstein, R., Atmospheric limitations to repeat-track radar interferometry, *Geophys. Res. Lett.*, 22, 2117-2520, 1995.
- Hauksson, E., L.M. Jones, K. Hutton, and D. Eberhart-Phillips, The 1992, Landers earthquake sequence: seismological observations, *J. Geophys. Res.*, 98, 19,835-19,858, 1993.
- Hart, E.W., W.A. Bryant, and J.A. Treiman, Surface faulting associated with the June 1992 Landers earthquake, California, *Calif. Geol.*, 46, 10-16, 1993.
- Hudnut, K.W., Y. Bock, M. Cline, P. Fang, Y. Feng, et al., Coseismic displacements of the 1992 Landers earthquake sequence, *Bull. Seism. Soc. Am.*, 84, 806-816, 1994.
- Kanamori, H. and D. Anderson, Amplitude of the earth's free oscillations and long period characteristics of the earthquake source, *J. Geophys. Res.*, 80, 1075-1078, 1975.
- Li, V.C., S.H. Seale, and T. Cao, Postseismic Stress and Pore Pressure Readjustment and Aftershock Distributions, *Tectonophysics*, 144, 37-54, 1987.
- Li, Y.G., T.H. Henyey, and P.C. Leary, Seismic reflection constraints on the structure of the crust beneath the San Bernardino Mountains, Transverse Ranges, southern California, *J. Geophys. Res.*, 97, 8817-8830, 1992.
- Li, Y.G., W.L. Ellsworth, C.H. Thurber, P.E. Malin, and K. Aki, Fault-Zone Guided Waves from Explosions in the San Andreas Fault at Parkfield and Cienega Valley, California, *Bull. Seism. Soc. Am.*, 87, 210-221, 1997.
- Linde, A.T., K. Suyehiro, S. Miura, I.S. Sacks, and A. Takagi, Episodic aseismic earthquake precursors, *Nature*, 334, 513-515, 1988.
- Lockner, D.A., and J.D. Byerlee, Dilatancy in hydraulically isolated faults and the suppression of instability, *Geophys. Res. Lett.*, 21, 2353-2356, 1994.
- MacKenzie, J.K., The elastic constants of a solid containing spherical holes, *Proc. Phys. Soc. London, B*, 63, 1-11 (1950).

- Massonnet, D., M. Rossi, C. Carmona, F. Adragna, G. Peltzer, K. Feigl, and T. Rabaute, The displacement field of the Landers earthquake mapped by radar interferometry, *Nature*, 364, 6433, 138-142, 1993.
- Massonnet, D., W. Thatcher, and H. Vadon, Detection of postseismic fault-zone collapse following the Landers earthquake, *Nature*, 612-616, 1996.
- Micheline and Mc Evilly, Seismological studies at Parkfield, I. Simultaneous inversion for velocity structure and hypocenters using cubic B-splines parametrisation, *Bull. Seism. Soc. Am.*, 81, 524-552, 1997.
- Muir-Wood, R. and G.C.P. King, Hydrological signatures of Earthquake Strain, *J. Geophys. Res.*, 98, 22,035-22,068, 1993.
- Murakami, M., M. Tobita, S. Fujiwara, T. Saito, and H. Masaharu, *J. Geophys. Res.*, 101, 8605-8614, 1996.
- Nur, A. and J. R. Booker, Aftershocks caused by pore fluid flow?, *Science*, 175, 885-887, 1971.
- Peltzer, G., K. W. Hudnut and K. Feigl, Analysis of coseismic surface displacement gradients using radar interferometry: New insights into the Landers earthquake, *J. Geophys. Res.*, 99, 21,971-21,981, 1994.
- Peltzer, G. and P. Rosen, Surface displacement of the 17 May 1993 Eureka Valley, California, earthquake observed by SAR interferometry, *Science*, 268, 1333-1336, 1995.
- Peltzer, G., P. Rosen, F. Rogez, and K. Hudnut, Fault creep and slow deformation processes detected with SAR interferometry, *EOS Trans. AGU*, 77, F49, 1996a.
- Peltzer, G., P. Rosen, F. Rogez, and K. Hudnut, Postseismic rebound in fault step-overs caused by pore fluid flow, *Science*, 273, 1202-1204, 1996b.
- Pollitz, F.F., Gravitational viscoelastic postseismic relaxation on a layered spherical Earth, *J. Geophys. Res.*, 102, 17,921-17,941, 1997.

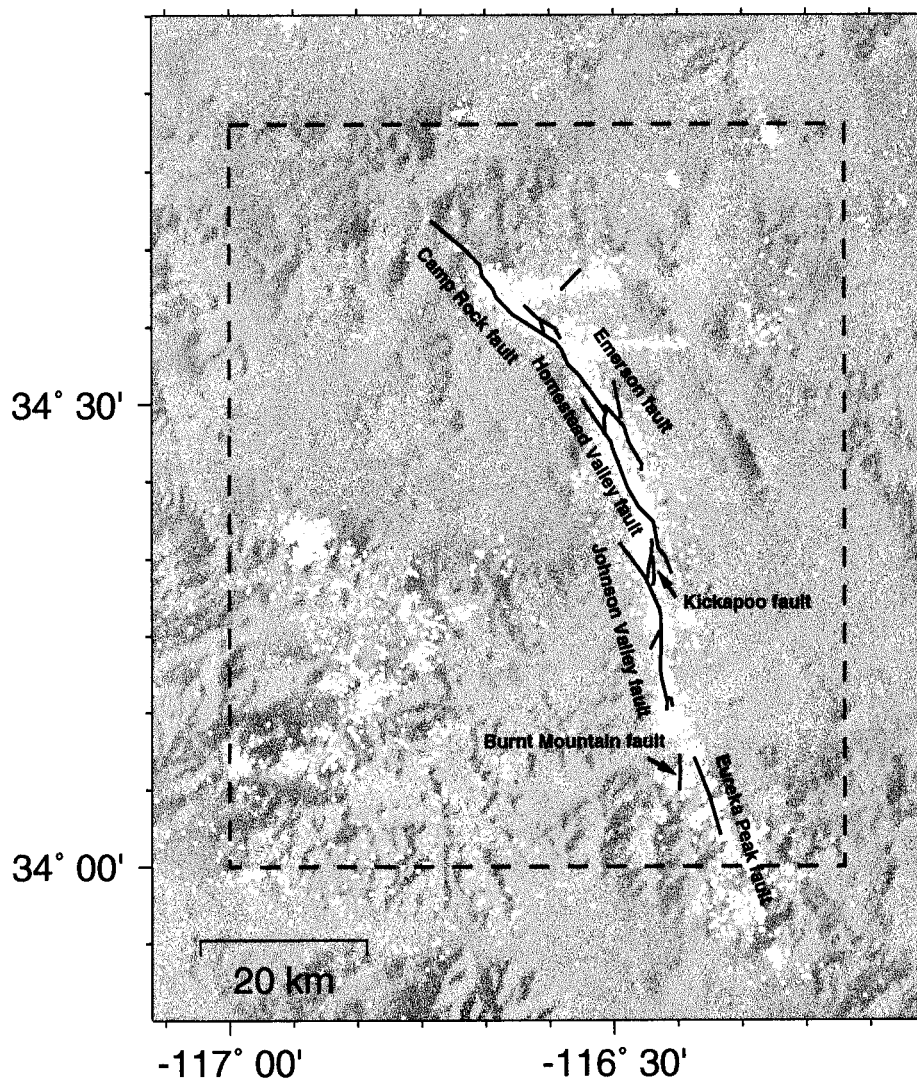
- Rice, J.R. and M.P. Cleary, Some basic stress diffusion solutions for fluid-saturated elastic porous media with compressible constituents, *Rev. Geophys. and Space Phys.*, 14, 227-241, 1976.
- Rosen, P., S. Hensley, Y. Lou, S. Shaffer, E. Fielding, A digital elevation model from Oregon to Mexico derived from SIR-C radar interferometry, *EOS Trans. suppl.*, AGU, 76, F64, 1995.
- Rudnicki, J.W. and C.H. Chen, Stabilization of rapid frictional slip on a weakening fault by dilatant hardening, *J. Geophys. Res.*, 93, 4745-4757, 1988.
- Sato, Y., Velocity of elastic waves propagated in media with small holes, *Tokyo Univ. Bull. Earthq. Res. Inst.*, 30, 178-190, 1952.
- Sauber, J., W. Thatcher, S.C. Solomon, and M. Lisowski, *Nature*, 367, 264-266, 1994.
- Savage, J.C., M. Lisowski, and W.H. Prescott, An apparent shear zone trending north-northwest across the Mojave Desert into Owens Valley, eastern California, *Geophys. Res. Lett.*, 17, 2113-2116, 1990.
- Savage, J.C., and J.L. Svarc, Postseismic deformation associated with the 1992 Mw=7.3 Landers earthquake, southern California, *J. Geophys. Res.*, 102, 7565-7577, 1997.
- Shen, Z.K., D. Jackson, Y. Feng, M. Cline, M. Kim, P. Fang, and Y. Bock, Postseismic deformation following the Landers earthquake, California, 28 June 1992, *Bull. Seism. Soc. Am.*, 84, 780-791, 1994.
- Shifflett, H., R. Whitbaard, Premonitory precursors to the Landers earthquake, *Eos Trans. Suppl.*, AGU, 76, 359-360, 1995.
- Sieh, K., L. Jones, E. Haukson, K. Hudnut, D. Eberhart-Phillips, T. Heaton, S. Hough, K. Hutton, H. Kanamori, A. Lilje, S. Lindvall, S. McGill, J. Mori, C. Rubin, J. Spotila, J. Stock, Hong Kie Thio, J. Treiman, B. Wernicke, and J. Zachariasen, Near-field investigations of the Landers earthquake sequence, April to July 1992, *Science*, 260, pp171-176, 1993.

- Sleep, N.H., and M.L. Blanpied, Creep, compaction and the weak rheology of major faults, *Nature*, 359, 687-692, 1992.
- Sleep, N.H., and M.L. Blanpied, Ductile creep and compaction: A mechanism for transiently increasing fluid pressure in mostly sealed fault zones, *Pageoph.*, 143, 1-40, 1994.
- Sowers, J.M., J.R. Unruh, W.R. Lettis, and T.D. Rubin, Relationship of the Kickapoo fault to the Johnson Valley and Homestead Valley faults, San Bernardino County, California, *Bull. Seism. Soc. Am.*, 84, 528-536, 1994.
- Spotila, J. A., and K. Sieh, Geologic investigation of a "slip gap" in the surficial ruptures of the 1992 Landers earthquake, southern California, *J. Geophys. Res.*, 100, 545-559, 1995.
- Sylvester, A., Investigation of nearfield postseismic slip following the Mw 7.3 Landers earthquake sequence of 28 June 1992, California, *Geophys. Res. Lett.*, 20, 1079-1082, 1993.
- Thurber C., Creep events preceeding small to moderate earthquakes on the San Andreas fault, *Nature*, 380, 425-428, 1996.
- Wald, D.J. and T.H. Heaton, Spatial and temporal distribution of slip for the 1992, Landers, California earthquake, *Bull. Seism. Soc. Am.*, 84, 668-691, 1994.
- Wdonwinski, S., Y. Bock, J. Zhang, P. Fang, and J. Genrich, Southern California Permanent GPS Geodetic Array: Spatial filtering of daily position for estimating coseismic and postseismic displacement induced by the 1992 Landers earthquake, *J. Geophys. Res.*, 102, 18,057-18,070, 1997.
- Yu, T.T., J.B. Rundle, and, J. Fernandez, Surface deformation due to a strike-slip fault in an elastic gravitational layer overlying a viscoelastic gravitational half-space, *J. Geophys. Res.*, 101, 3199-3214, 1996.

Zebker, H.A., C. Werner, P. Rosen, and S. Hensley, Accuracy of topographic maps derived from ERS-1 interferometric radar, *IEEE Trans. Geosc. and Rem. Sens.*, 32, 823-836, 1994a.

Zebker, H. A., P. Rosen, R.M. Goldstein, A. Gabriel, and C.L. Werner, On the derivation of coseismic displacement fields using differential radar interferometry: the Landers earthquake, *J. Geophys. Res.*, 99, 617-634, 1994b.

Zebker, H.A., P. A. Rosen, and S. Hensley, Atmospheric effects in interferometric synthetic-aperture radar surface deformation and topographic maps, *J. Geophys. Res.*, 102, 7547-7563, 1997.



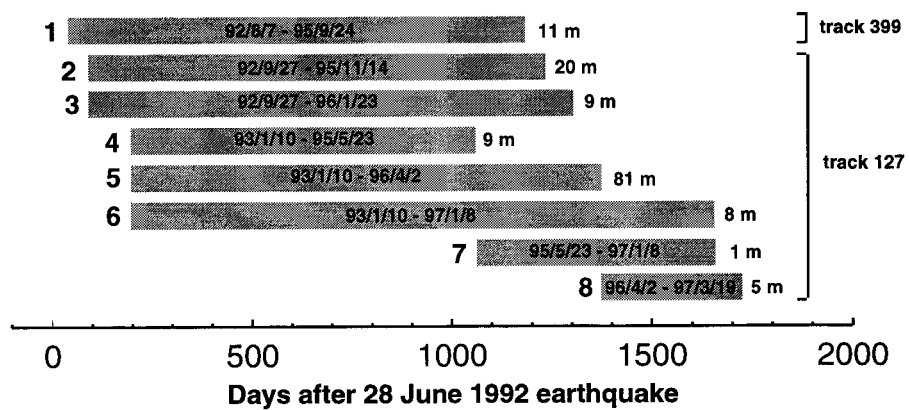
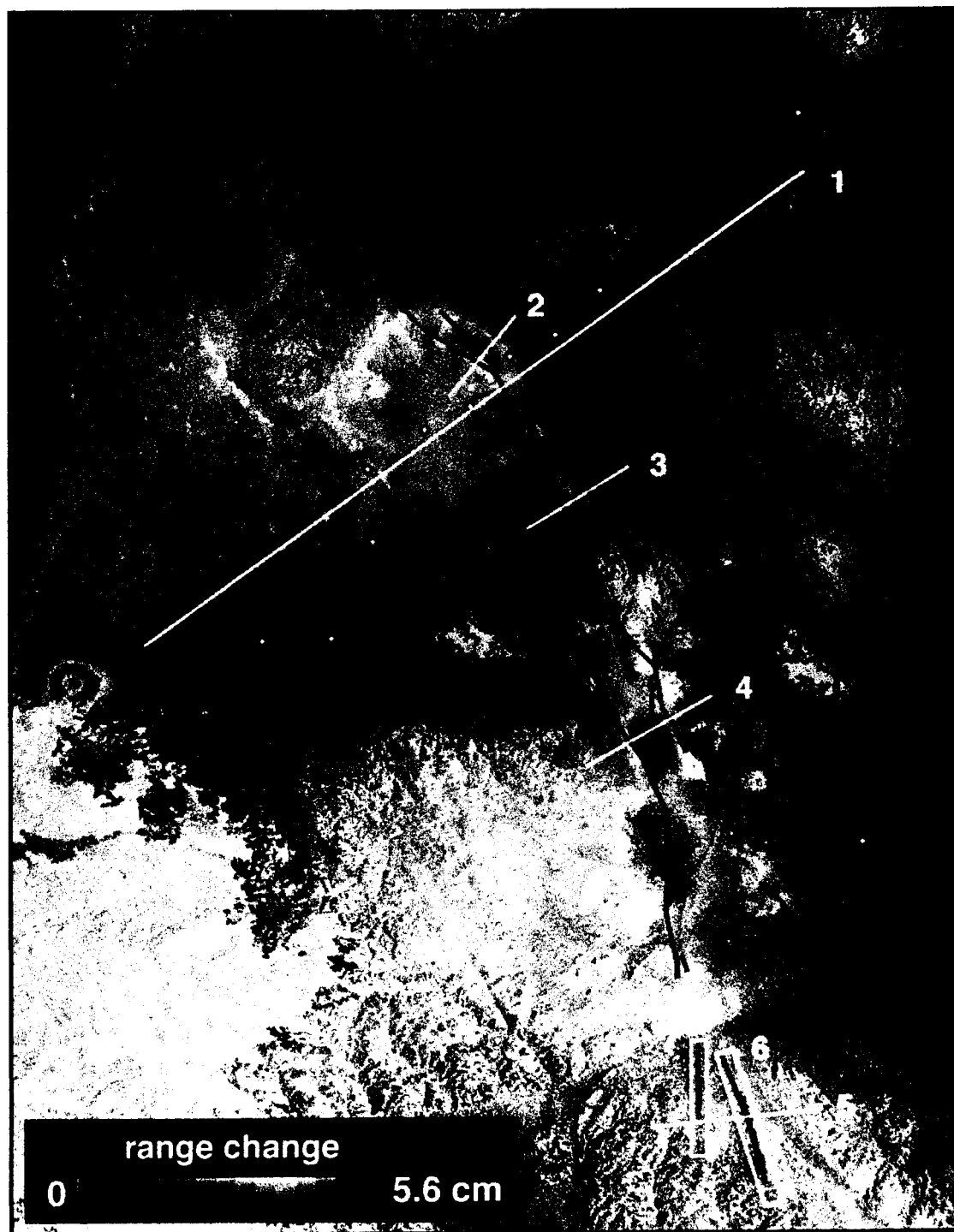
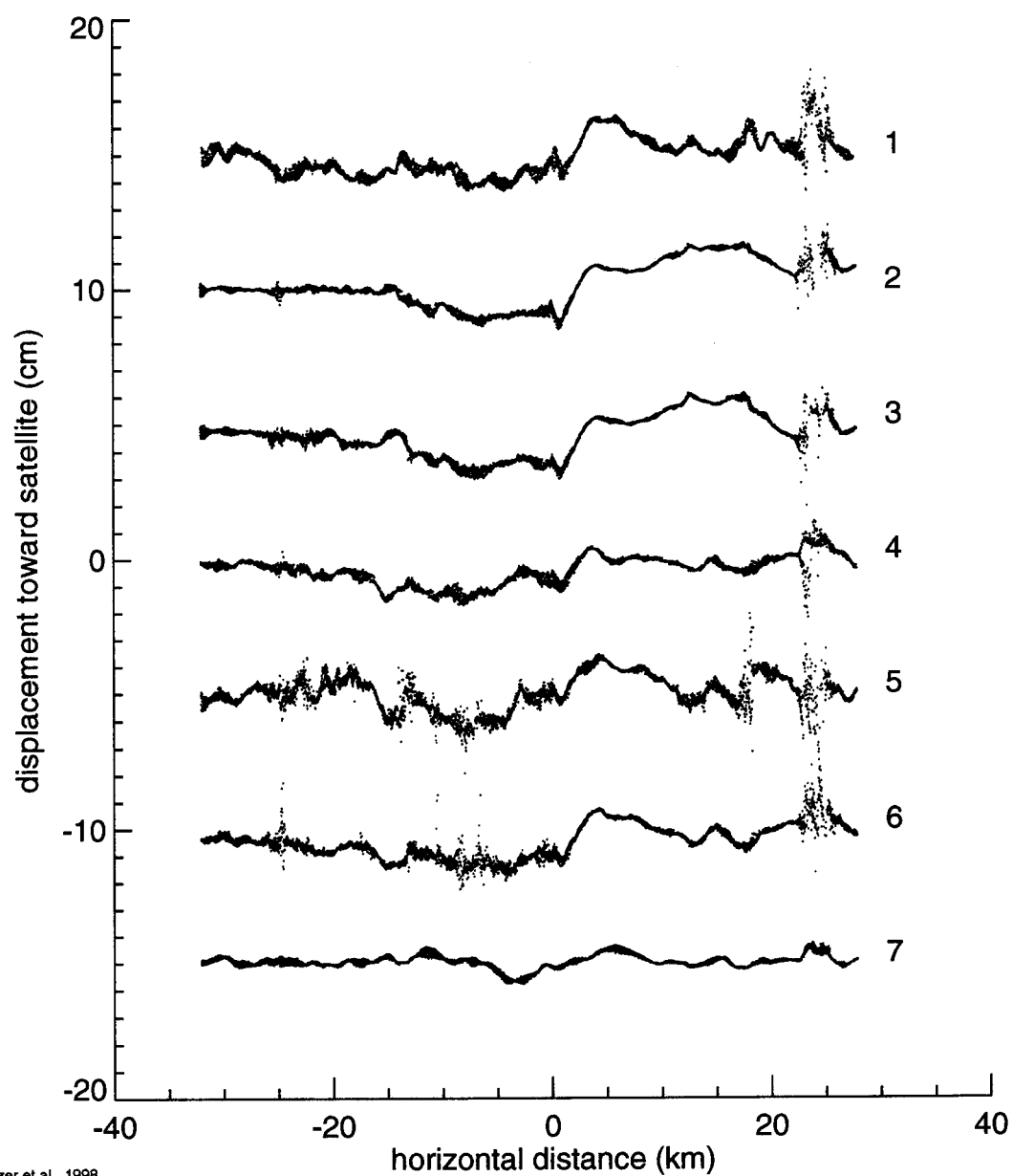


Figure 2, Peltzer et al., 1998





Figure, 4 - Peltzer et al., 1998

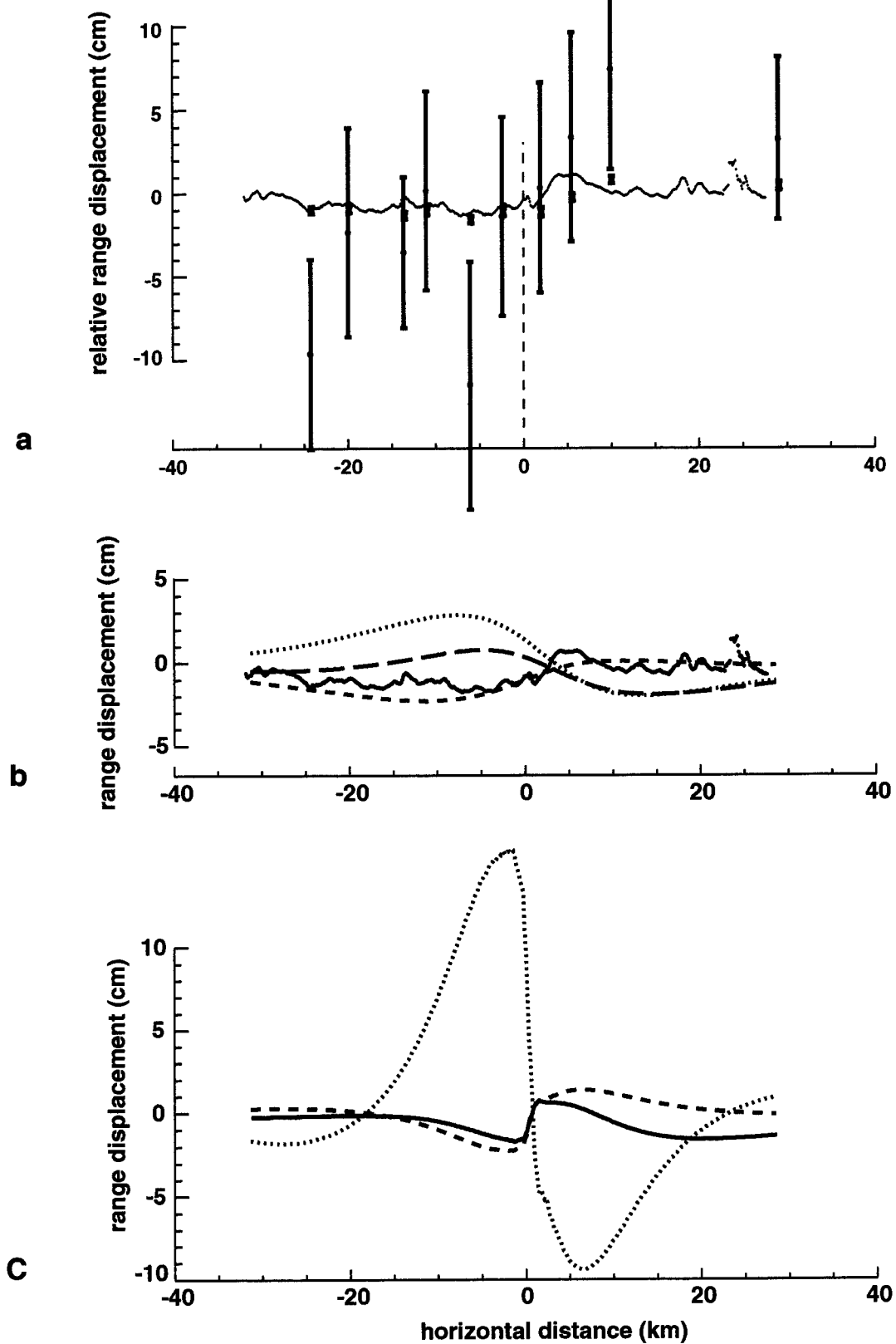


Figure 5
Peltzer et al., 1998

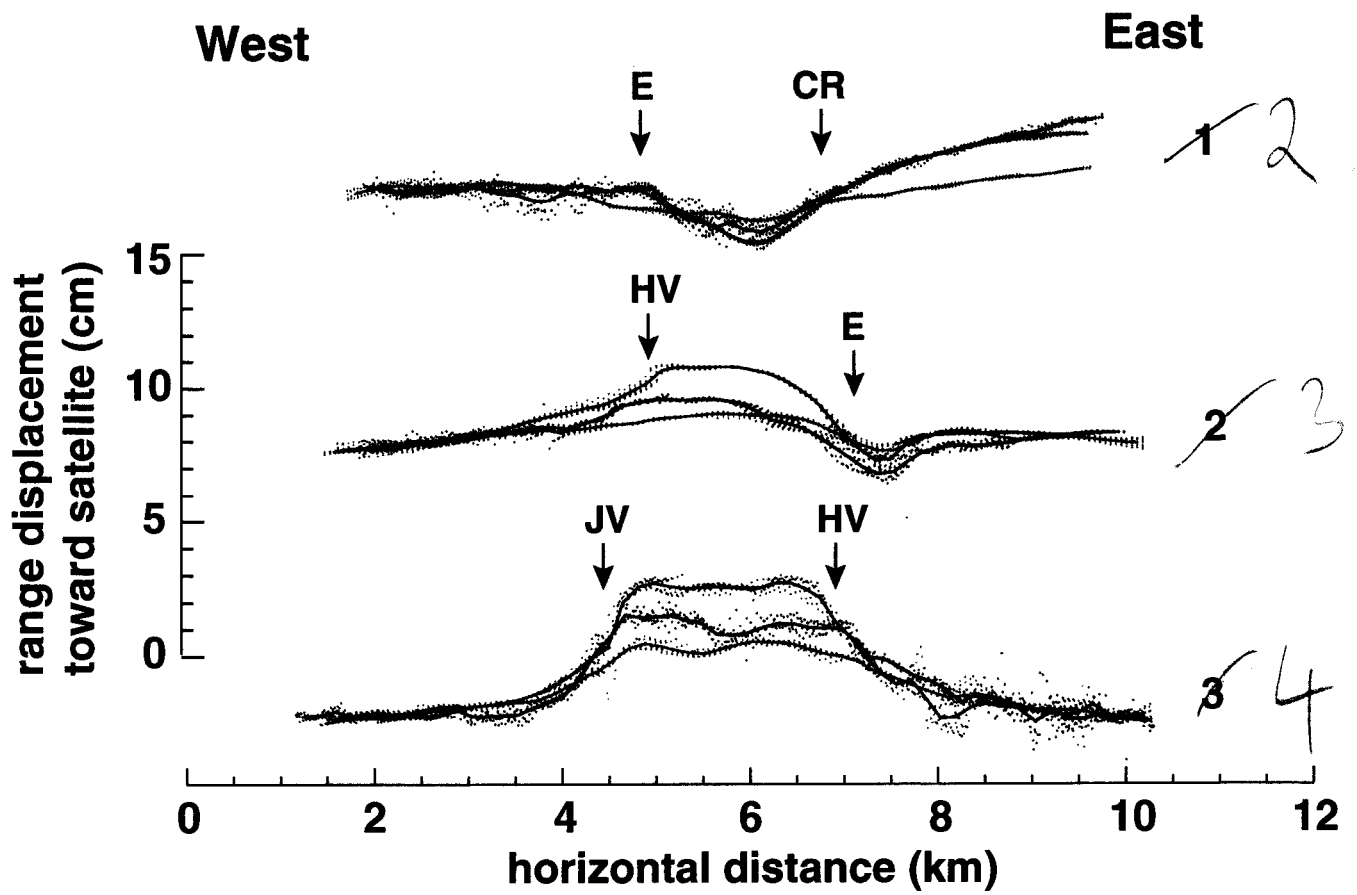


Figure 6 - Peltzer et al., 1998

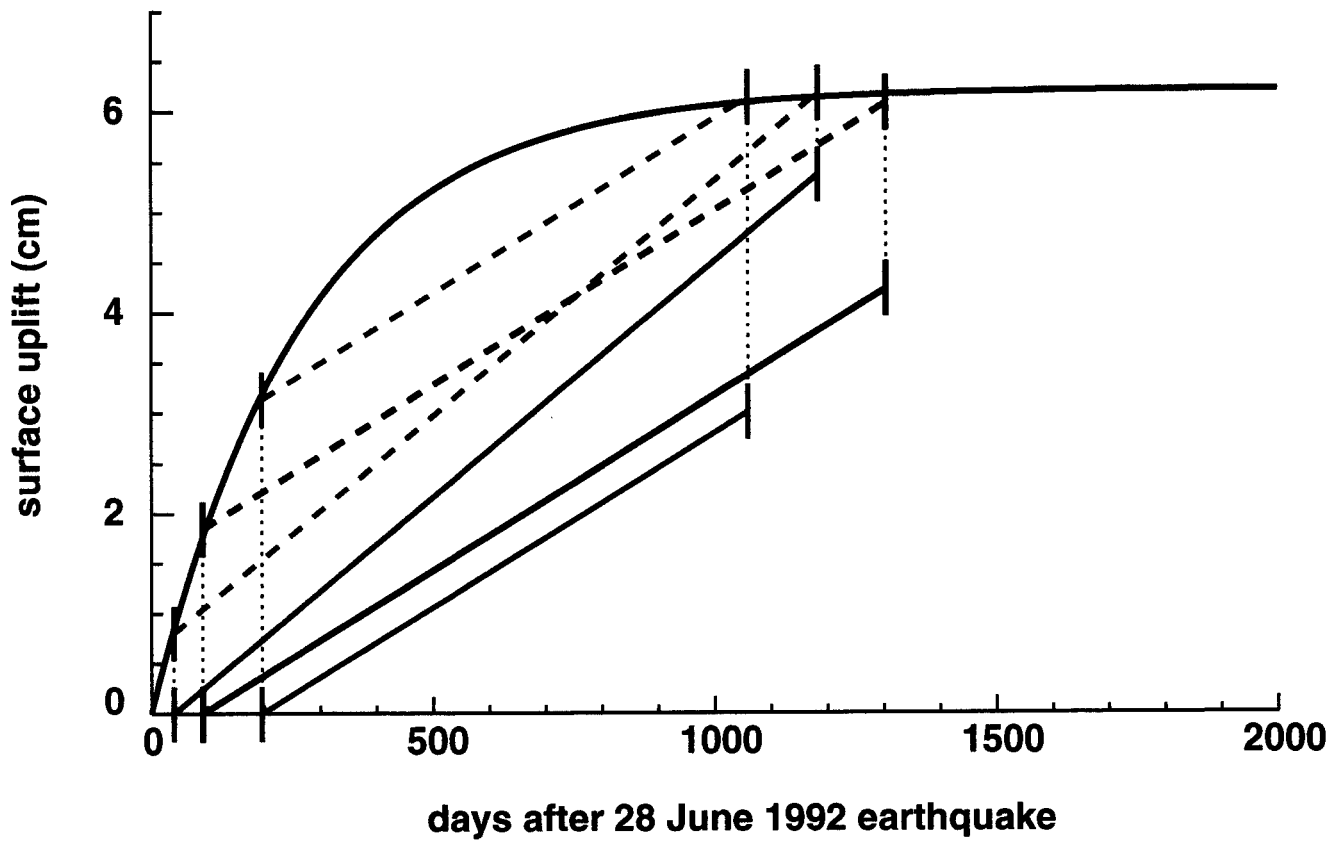


Figure 7 - Peltzer et al., 1998

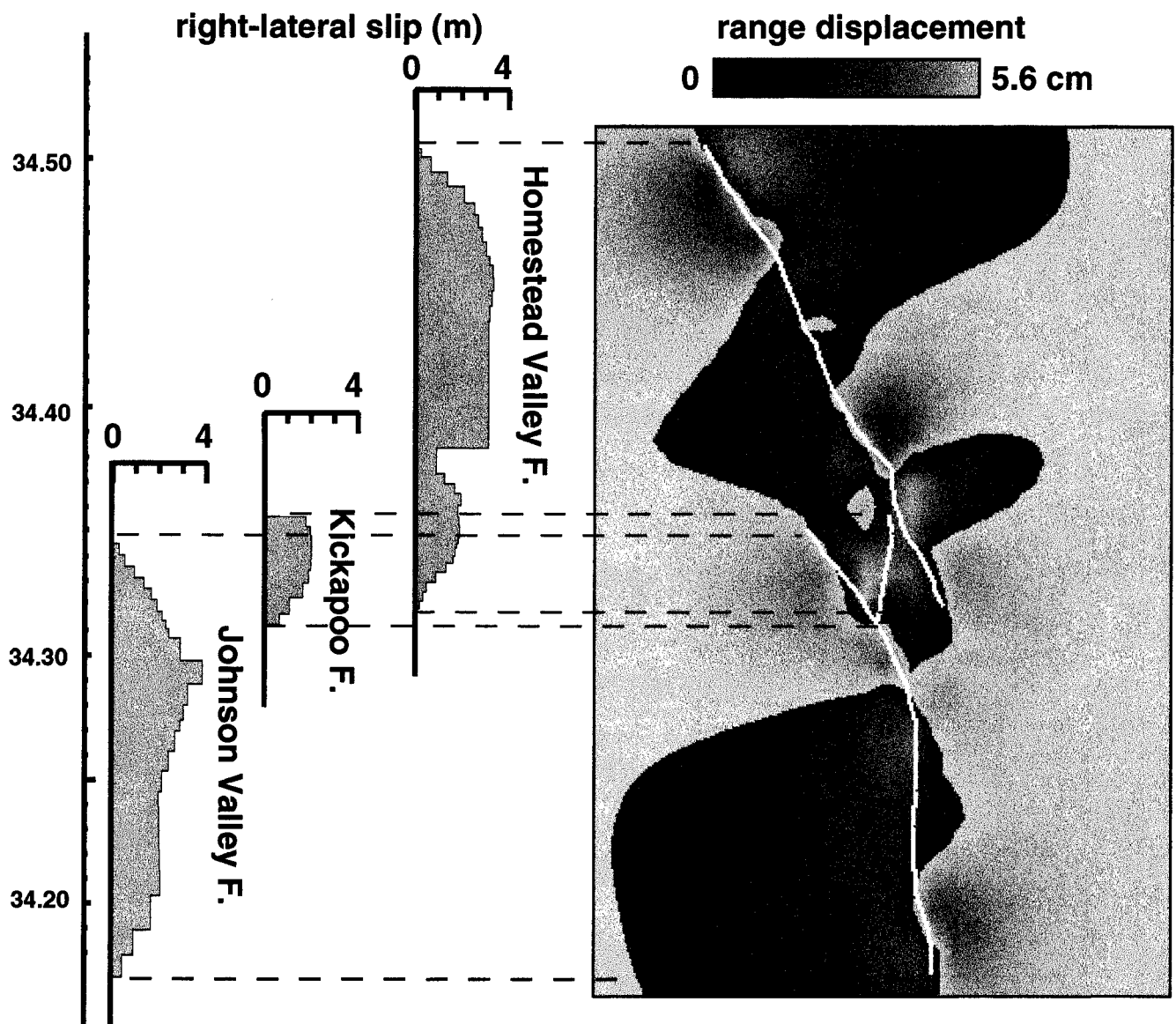


Figure 8a - Peltzer et al., 1997

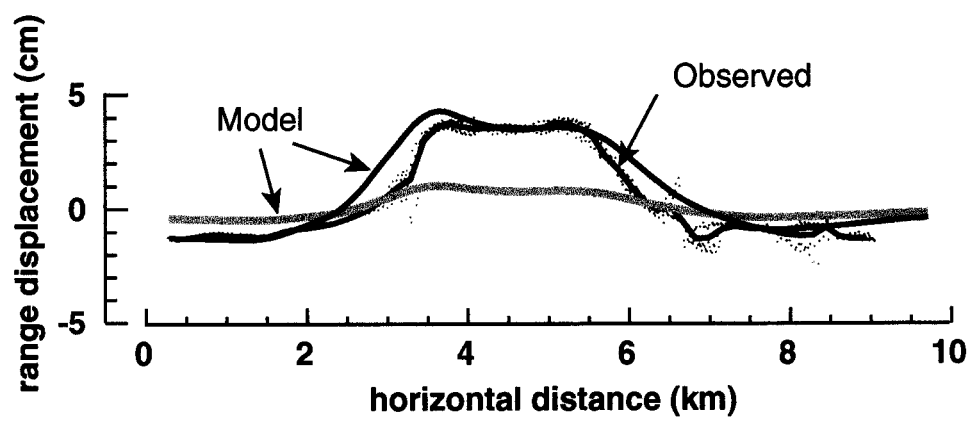


Figure 8b - Peltzer et al., 1998

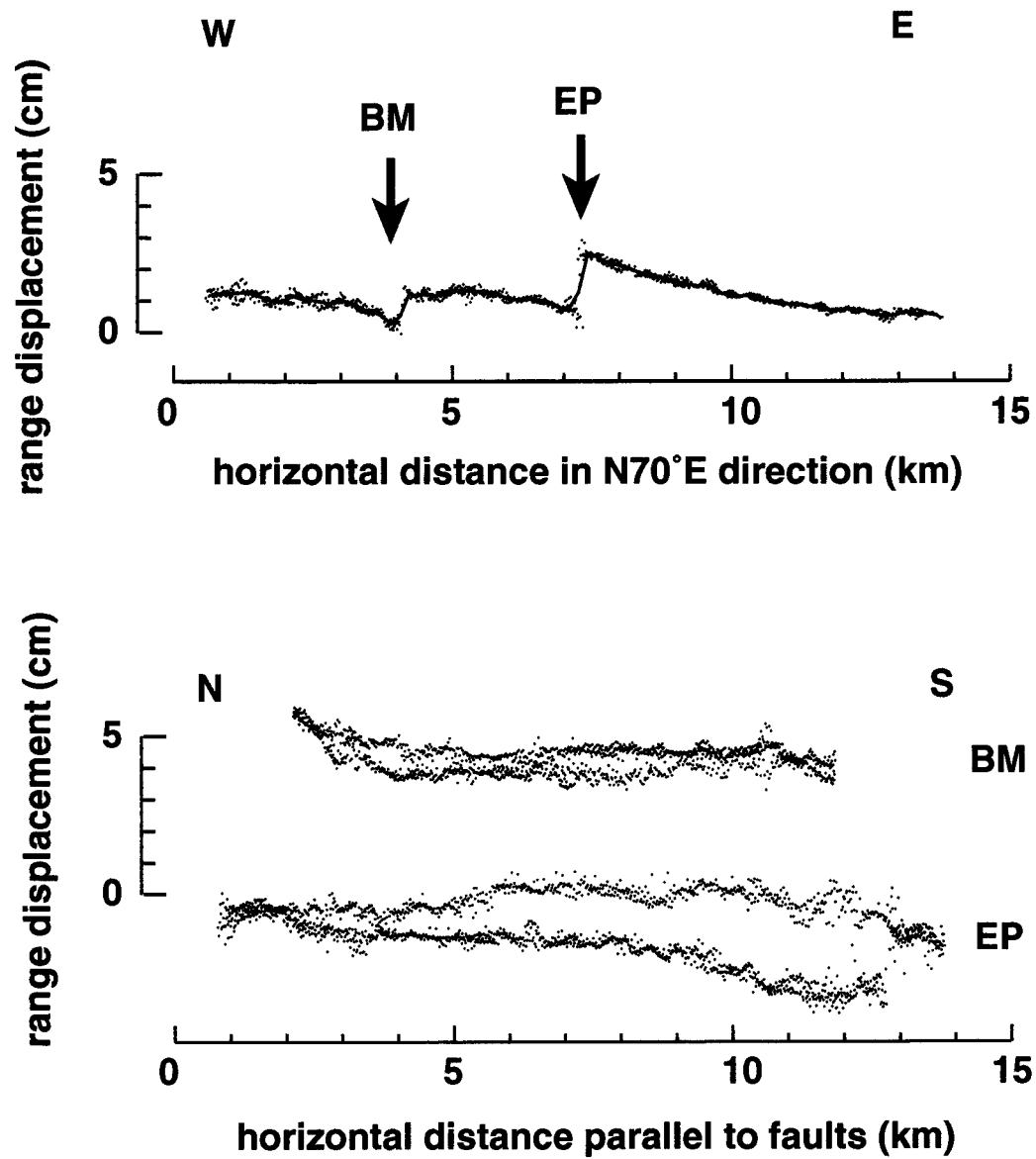


Figure 9a - Peltzer et al., 1998

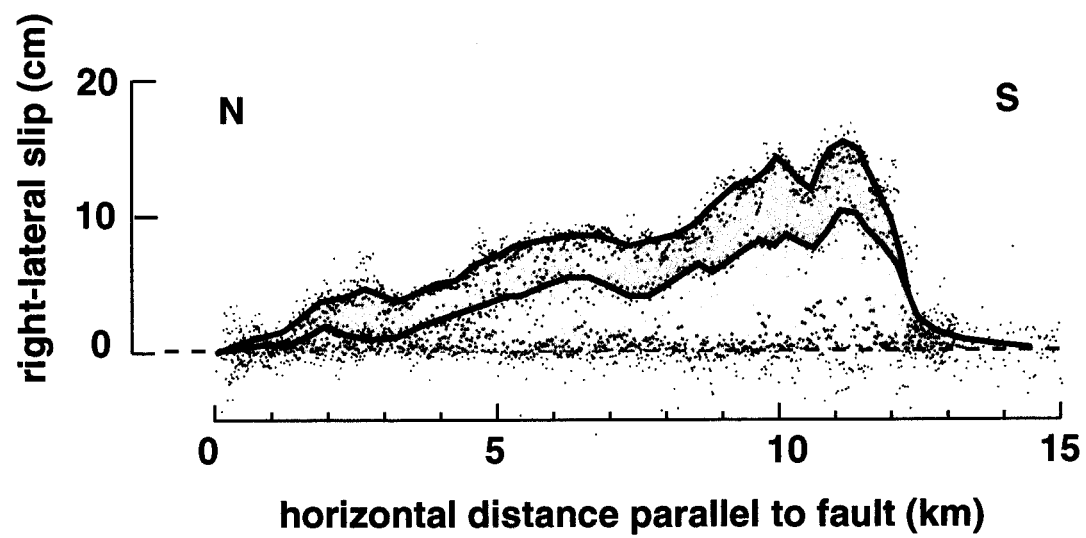


Figure 9b - Peltzer et al., 1998

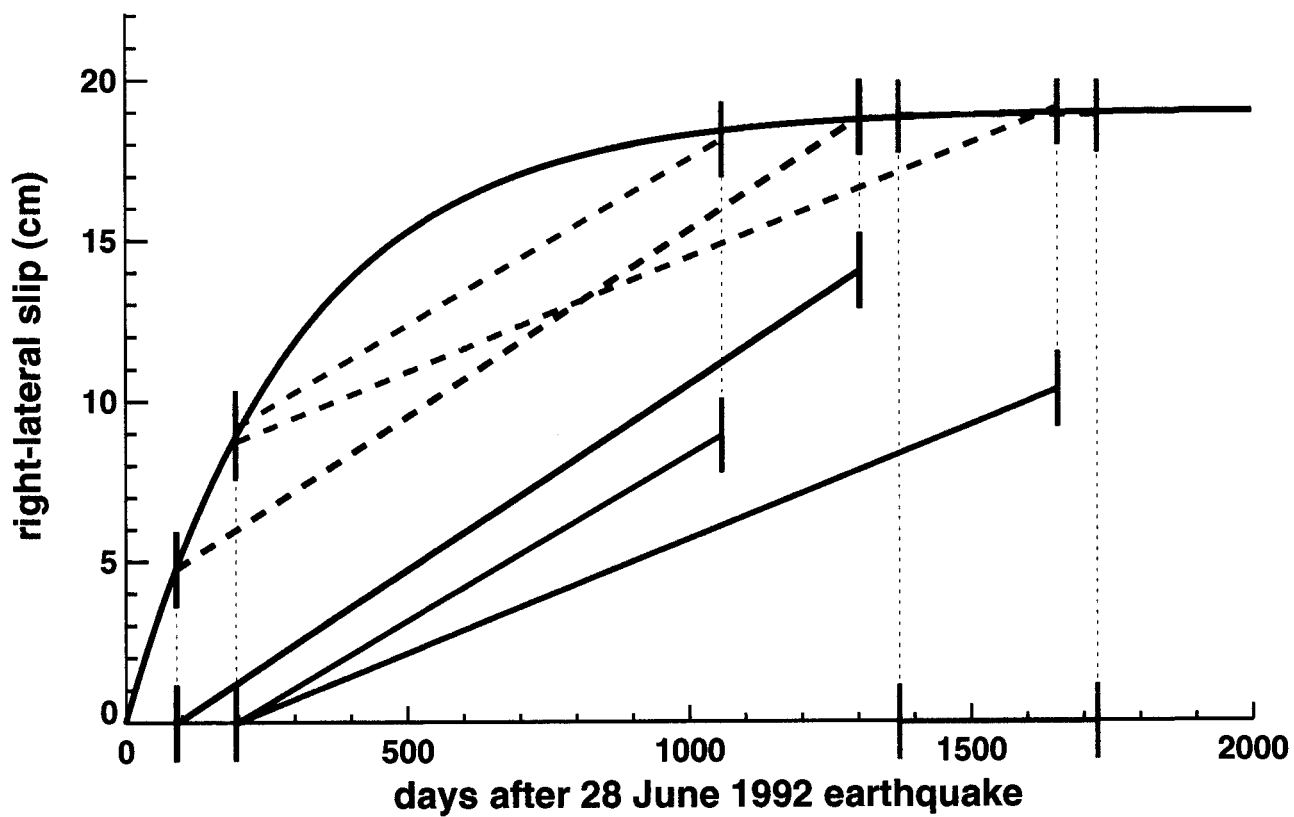


Figure 10 - Peltzer et al., 1998

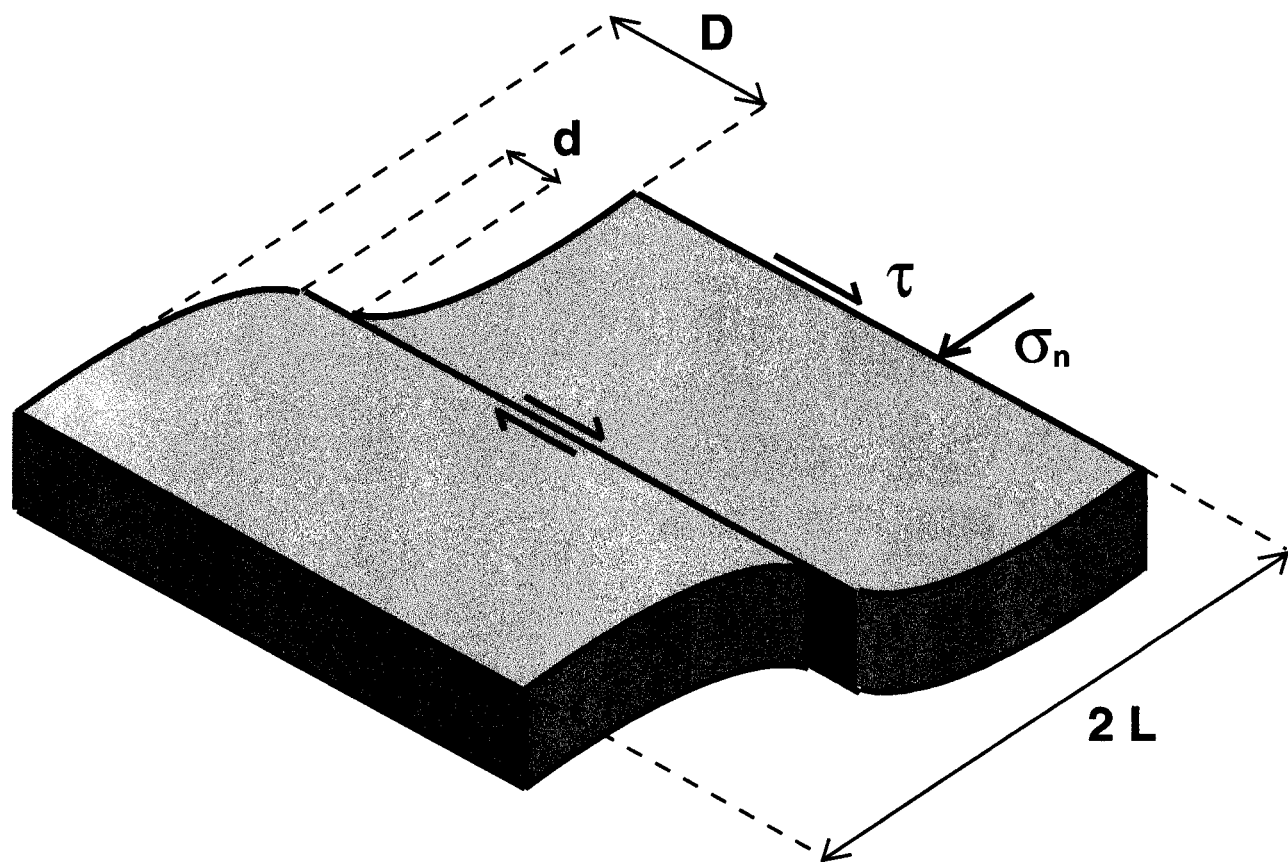


Figure 11 - Peltzer et al., 1998